Science Bulletin 70 (2025) 1581–1585

Contents lists available at ScienceDirect

Science Bulletin

journal homepage: www.elsevier.com/locate/scib

Short Communication

Accurate identification and formation mechanism unraveling of radicals in UV-induced peracetic acid activation system using *in-situ* electron paramagnetic resonance

Long Chen [a], Ruohan Zhang [a], Zhaoli Liu [a], Fan Li [a,b], Boyu Huang [a], Wen Liu [a,c,*]

[a] College of Environmental Sciences and Engineering, The Key Laboratory of Water and Sediment Sciences, Peking University, Beijing 100871, China
[b] Beijing Key Lab for Source Control Technology of Water Pollution, College of Environmental Science and Engineering, Beijing Forestry University, Beijing 100083, China
[c] Molecular Sciences National Laboratory for Molecular Sciences, Peking University, Beijing 100871, China

ARTICLE INFO

Article history:
Received 7 November 2024
Received in revised form 6 January 2025
Accepted 20 February 2025
Available online 8 March 2025

Advanced oxidation processes (AOPs) have drawn intensive attention in wastewater treatment areas for the efficient degradation of organic pollutants owing to abundant reactive species production and rapid reaction kinetics [1]. Among them, AOPs based on peracetic acid ($CH_3C(=O)OOH$, PAA), which is applied as a substitute for H_2O_2, have been considered as a promising technology recently [2]. Compared with H_2O_2 (1.45 Å and 213 kJ mol^{-1}), the longer bond length (1.49 Å) and lower bond energy (159 kJ mol^{-1}) of peroxy bond in PAA result in easier activation to generate radicals [2,3]. Therefore, the oxygen-centered radicals including hydroxyl radical (·OH), alkoxy radicals such as acetylperoxyl radical ($CH_3C(=O)OO·$) and acetyloxyl radical ($CH_3C(=O)O·$), as well as carbon-centered radicals like methyl radical ($·CH_3$), will be produced after activation [4]. In addition, some secondary radicals such as hydrogen peroxide radical (·OOH), $CH_3·CHOH$, and $CH_3·C(=O)$ can also be generated after radical-chain reactions in water [4]. UV light can realize homogeneous PAA activation through the generation of excited triplet states, where the difference in produced radicals generally results from the induced activation routes by different lights [5]. Specifically, PAA activation induced by UV light (254 nm) declares that ·OH, $CH_3C(=O)OO·$, and $CH_3C(=O)O·$ are formed and dominantly contribute to organic pollutants degradation [6], among which $CH_3C(=O)OO·$ is calculated as the most abundant radical according to kinetic modeling [4]. Thus, it holds great importance to clearly understand the reaction characteristics of produced radicals and their transformation behaviors in UV-induced PAA (UV/PAA) AOPs, so accurate identification of the produced radicals is the prerequisite knowledge [7].

A fact is that it is very hard to provide direct evidence of the existence of radicals (especially alkoxy and alkyl radicals) in PAA-based AOPs, considering their complicated production and transformation behaviors [8]. Recent studies mainly focus on the degradation efficiency of organic pollutants, but solid evidence on the generation of different radicals is lacking [9,10]. The widely used scavenger quenching experiments cannot directly verify the presence of radicals [7]. Moreover, although electron paramagnetic resonance (EPR) spectroscopy can directly obtain radical signals with spin-trapping reagents like 5,5-dimethyl-1-pyrrolidine-*N*-oxide (DMPO), precise capture and analysis of EPR spectra still pose challenges for accurate identification due to the variety of species and complicated transformation process [11]. It is impressive that the development of computational calculation methods may take new insights into the radical formation and transformation mechanism. Theoretical calculation is a widely used and powerful tool in chemistry, offering deep insights into reaction mechanisms and intermolecular interactions, particularly in cases where experimental conditions are challenging to fully control or directly observe. Among them, a theoretical calculation based on density functional theory (DFT) is an efficient and versatile computational method that can provide reliable predictive results across a wide range of chemical systems [12]. For UV/PAA AOPs, DFT calculation can provide orbital energy level and charge distribution information, providing visual analysis on excited state transitions and radical formation process [12].

Herein, we developed an *in-situ* EPR method to accurately identify the radicals produced in UV/PAA systems. UV light irradiation

* Corresponding author.
E-mail address: wen.liu@pku.edu.cn (W. Liu).

https://doi.org/10.1016/j.scib.2025.03.008

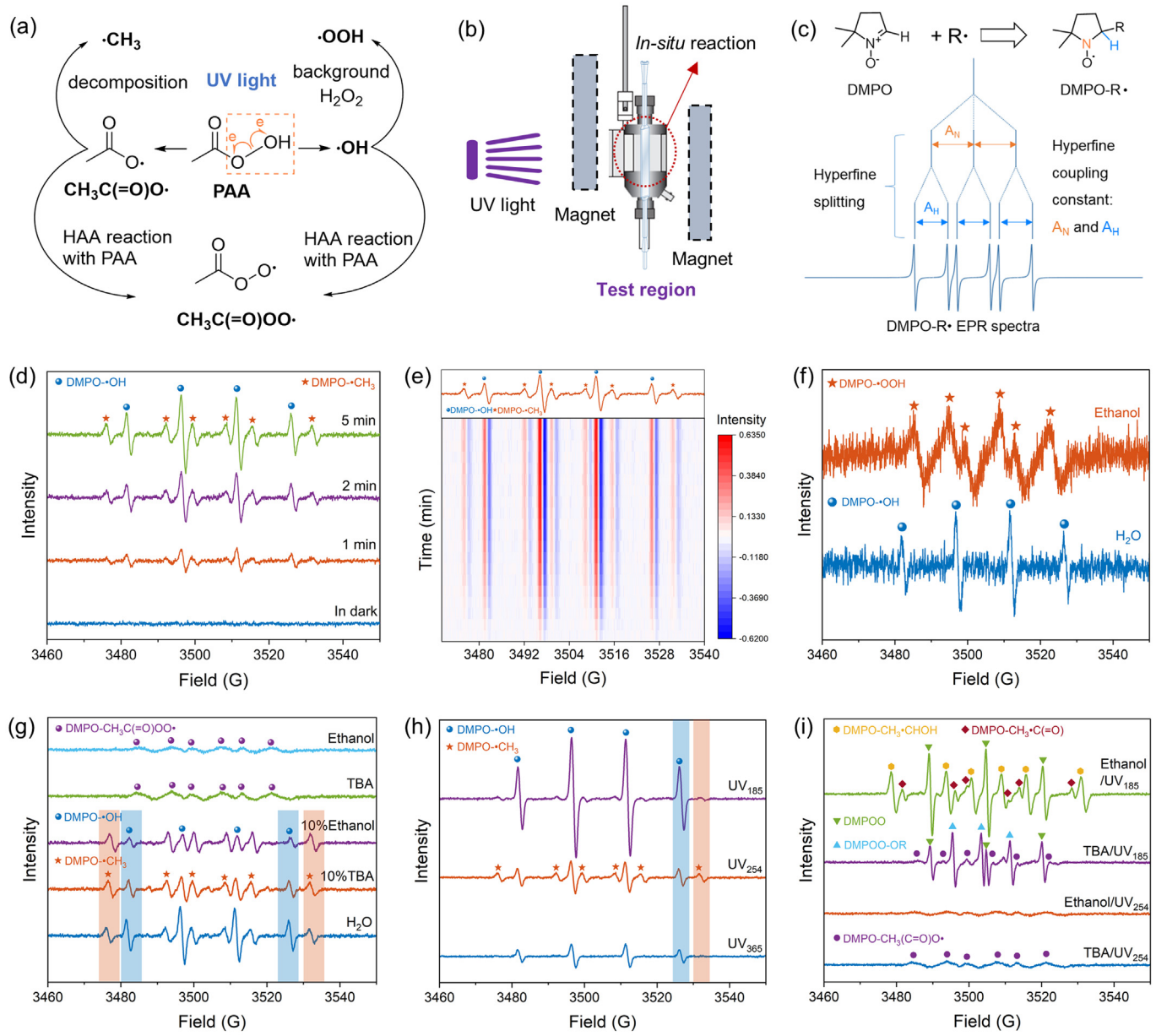

Fig. 1. *In-situ* EPR workflow and radical identification in UV-induced PAA activation systems. (a) PAA activation and radical generation reactions in UV/PAA system. (b) *In-situ* EPR analytical system equipped with UV light. (c) Radical capture process and hyperfine splitting coupling of DMPO adducts, where "R" represents the radical functional group such as OH, CH_3, and $CH_3C(=O)OO\cdot$ (d) EPR spectra of radicals in UV_{254}/PAA system captured by DMPO in water. (e) The hot map of captured DMPO-·OH and DMPO-·CH_3 signals in UV_{254}/PAA system in water. (f) EPR signals of radicals in UV_{254}/H_2O_2 system captured by DMPO in water and ethanol solution. (g) EPR spectra of radicals in UV_{254}/PAA system captured by DMPO in organic solvents. (h) Captured radical signals in UV/PAA systems with different light wavelengths in water. (i) Captured radical signals in UV_{254}/PAA and UV_{185}/PAA systems in different organic solvents. Test conditions: [PAA] or $[H_2O_2]$ = 10.0 mmol L^{-1}, [DMPO] = 100 m mol L^{-1}, pH 5, light intensity = 10 mW cm^{-2}.

at wavelengths of 185, 254, and 365 nm was conducted for PAA activation and generation of radicals (Fig. 1a), which are the three most used UV-AOPs in the water treatment area. DMPO was used to track the different radicals and corresponding measurement conditions were systematically established. The *in-situ* EPR system equipped with UV light source and reactant injector was constructed to track the signals of generated radicals (Fig. 1b). The simulation and analysis of EPR signals were carried out on MATLAB software and EasySpin package based on the hyperfine coupling constants of DMPO adducts (A_N and A_H) (Fig. 1c). DFT calculation was further employed to deeply unravel the PAA activation mechanism under UV light irradiation. This work can greatly advance the understanding of complicated radical behaviors in UV/PAA systems, and the aim of this study is to achieve: (1) accurate identification and *in-situ* analysis of complex radicals (especially alkoxy and alkyl radicals) in PAA-based AOPs activated by UV lights with different wavelengths; (2) clear illustration the generation mechanism and the process of key radicals in UV/PAA systems by means of DFT calculations.

The molar absorption coefficient of PAA was determined as 10.01 mol L^{-1} cm^{-1} (254 nm), with a higher quantum yield of 1.20 mol $Einstein^{-1}$ than that of H_2O_2 (18.7 mol L^{-1} cm^{-1}, 0.5 mol $Einstein^{-1}$) for light activation [6]. Therefore, at the same concentration, the homogeneous cleavage of PAA was the predominant photolysis pathway to generate radicals (Eq. (1)). In water, PAA did not react with DMPO in dark, and thus no signals were

observed (Fig. 1d). Under UV light irradiation at 254 nm (UV_{254}), the signals assigned to DMPO-·OH and DMPO-·CH_3 were detected. The typical quartet signal with the intensity ratio of 1:2:2:1 corresponded to DMPO-·OH ($A_N = A_H = 14.9$ G), while the six equidistant peaks with the spectral feature of $A_N = 16.0$ G and $A_H = 23.6$ G were assigned to DMPO-·CH_3. Under light irradiation, the homogeneous cleavage of peroxy bond in PAA firstly occurs to produce $CH_3C(=O)O\cdot$ and ·OH (Eq. (1)), followed by hydrogen atom abstraction (HAA) reactions with PAA to generate $CH_3C(=O)OO\cdot$ (rate constant of 1×10^7 L mol^{-1} s^{-1} for Eq. (2) and 1.3×10^9 L mol^{-1} s^{-1} for Eq. (3)) [6]. $CH_3C(=O)O\cdot$ will also rapidly undergo unimolecular decomposition to form ·CH_3 with a high reaction rate constant of 2.3×10^5 s^{-1} [2], especially under UV light irradiation (Eq. (4)). Therefore, the existence of ·CH_3 can demonstrate the generation of $CH_3C(=O)O\cdot$ in the light activation system. With the increase of irradiation time, the signal intensity of DMPO-·OH and DMPO-·CH_3 synchronously increased (Fig. 1e). The lower intensity of DMPO-·CH_3 was attributed to ·CH_3 belonging to a secondary radical transformed from $CH_3C(=O)O\cdot$ (Eq. (3)), and ·CH_3 would be further oxidized to a peroxyl radical (·$OOCH_3$) after reacted with O_2 (reaction rate constant of 4.7×10^9 L mol^{-1} s^{-1}) (Eq. (5)).

$$CH_3C(=O)OOH \xrightarrow{UV} CH_3C(=O)O\cdot + \cdot OH \quad (1)$$

$$\cdot OH + CH_3C(=O)OOH \rightarrow CH_3C(=O)OO\cdot + H_2O \quad (2)$$

$$CH_3C(=O)O\cdot + CH_3C(=O)OOH \rightarrow CH_3C(=O)OO\cdot + CH_3(C=O)OH \quad (3)$$

$$CH_3C(=O)O\cdot \rightarrow \cdot CH_3 + CO_2 \quad (4)$$

$$\cdot CH_3 + O_2 \rightarrow \cdot OOCH_3 \quad (5)$$

$$H_2O_2 \xrightarrow{UV} 2 \cdot OH \quad (6)$$

$$\cdot OH + H_2O_2 \rightarrow \cdot OOH + H_2O \quad (7)$$

Meanwhile, the background H_2O_2 can also be activated by UV light to generate ·OH and subsequent ·OOH (Eqs. (6)–(7) and Fig. 1f). In water, only DMPO-·OH was detected in the UV_{254}/H_2O_2 system, and the relatively lower signal intensity than that in UV_{254}/PAA system was observed for a lower quantum yield. The contribution of DMPO-·OH from background H_2O_2 can be determined as only 17.6% through the ratio of signal intensity after EasySpin simulation (Fig. S1 online). It is worth noting that $CH_3C(=O)OO\cdot$ can also be recognized as a secondary radical transformed from ·OH/$CH_3C(=O)O\cdot$ reacting with PAA (Eqs. (2)–(3)). The difficulty in identifying these organic radicals lies in the slow capture rate by DMPO and the rapid conversion of DMPO adducts [11]. The introduction of organic solvents such as ethanol and *tert*-butyl alcohol (TBA) can achieve formation of DMPO adducts with a higher lifetime. After the addition of 10% TBA (v/v) in the test solution, the signals of DMPO-·OH and DMPO-·CH_3 were still observed, attributing to the photoinduced hydrolysis reaction of DMPO-$CH_3C(=O)OO\cdot$ (Fig. S2 online). A similar result was also obtained after the addition of 10% ethanol (v/v). The replacement of organic solvents was used to extend the lifetime of DMPO adducts or avoid the hydrolysis reaction of DMPO adducts. However, after the solvent was totally replaced from H_2O to TBA or ethanol, the signal of $CH_3C(=O)OO\cdot$ was clearly captured, with a characteristic parameter of 13.5 G for A_N and 9.0 G for A_H (Fig. 1g). Therefore, the identification of organic radicals needs different detection methods, where ·CH_3 and $CH_3C(=O)OO\cdot$ can be detected in water and alcohol solution (TBA or ethanol), respectively. Besides, all radicals may undergo coupling termination to form dimers, thereby terminating the radical chain reaction [2].

The activation of PAA and bond cleavage pathways are highly related to the input photon energy (i.e., different light wavelengths). Electronic excited state analysis is conducted to reveal the PAA activation mechanism after receiving photo-energy. In this study, some high-energy excited states of PAA would be generated in the UV_{185}/PAA activation system, which may not exist in the UV_{254}/PAA and UV_{365}/PAA systems with the lower photon energies, resulting in the generation of different types of radicals in the three UV/PAA systems. The EPR analysis effectively identified the types of radicals through hyperfine coupling constants, while DFT calculations based on excited-state theory can analyze the processes of radical generation under different UV wavelengths. PAA molecule will be excited to a singlet state after light absorption (Eq. (8)), then convert to a more stable triplet state with lower energy through intersystem crossing (Fig. 2a), thereby generating radicals. The highest occupied molecular orbital (HOMO) and the lowest unoccupied molecular orbital (LUMO) have been calculated (Fig. 2b). The LUMO and HOMO are distributed throughout the entire PAA molecule, not just in the peroxy bond region, with a LUMO-LUMO gap of 7.63 eV higher than the photo-energy of UV_{254} light (4.88 eV). The bond dissociation energy (BDE) of peroxy bond is further calculated as 44.8 kcal mol^{-1} (1.94 eV) using B3LYP/cc-pVTZ (Fig. S3 online), which is a little higher than the reported value (38 kcal mol^{-1}, 1.65 eV) using the Spartan program Model LSDA/pBP86/DN**. In comparison, the calculated BDE of the peroxy bond (1.94 eV) is much smaller than the photo-energy of UV_{254} light (4.88 eV). For the activation of PAA and bond cleavage, the photon energy must match the BDE, and the energy should be able to promote PAA molecule to a suitable excited state. The theoretical UV–vis absorbance spectra are obtained by excited states calculations using time-dependent density functional theory (TDDFT) (Fig. 2b), accompanied by the wavefunction information of orbitals. Additionally, the experimental UV–vis spectra of PAA also indicate that low light absorption at 254 nm was observed (Fig. S4 online). Theoretical calculation and experimental results both confirmed that PAA showed a main absorption peak at the light wavelength of < 254 nm. However, the limited light absorption would also allow PAA to capture photo energy, undergoing non-radiative relaxation and excited-state dissociation to generate radicals. The energy gap of the first singlet state (S1) of PAA is calculated to be 5.82 eV (213.1 nm) using TDDFT and corrected to 4.71 eV (263.3 nm) using the equation of motion-coupled cluster singles and doubles (EOM-CCSD). This directly indicated that PAA can be effectively excited by UV_{254} (4.88 eV) to generate ·OH and $CH_3C(=O)O\cdot$, which is consistent with the EPR result (Fig. 1d). The transition density of S1 state is mainly concentrated in the peroxy bond region (Fig. 2b). D index is calculated to measure the distance between the mass center of holes and electrons, which is quite small for the S1 state of PAA (0.31 Å), only 20.8% of the length of peroxy bond (1.49 Å) (Fig. 2c). However, the larger Sr index (0.51) measuring the degree of overlap between holes and electrons indicates a 51% overlap, similar to the spectra of charge density difference (Fig. S5a online) [13]. σ_{hole} and $\sigma_{electron}$ indexes (measuring the overall distribution breadth) show a similar spin distribution breadth of holes and electrons (Fig. S5b online), further confirming the local excitation process of S1 state. The major transitions sorted by absolute contributions to S1 state are calculated in Fig. 2d, where the transition from HOMO to the molecular orbitals of MO27 (22.9%), MO29 (18.9%), MO30 (16.8%), MO22

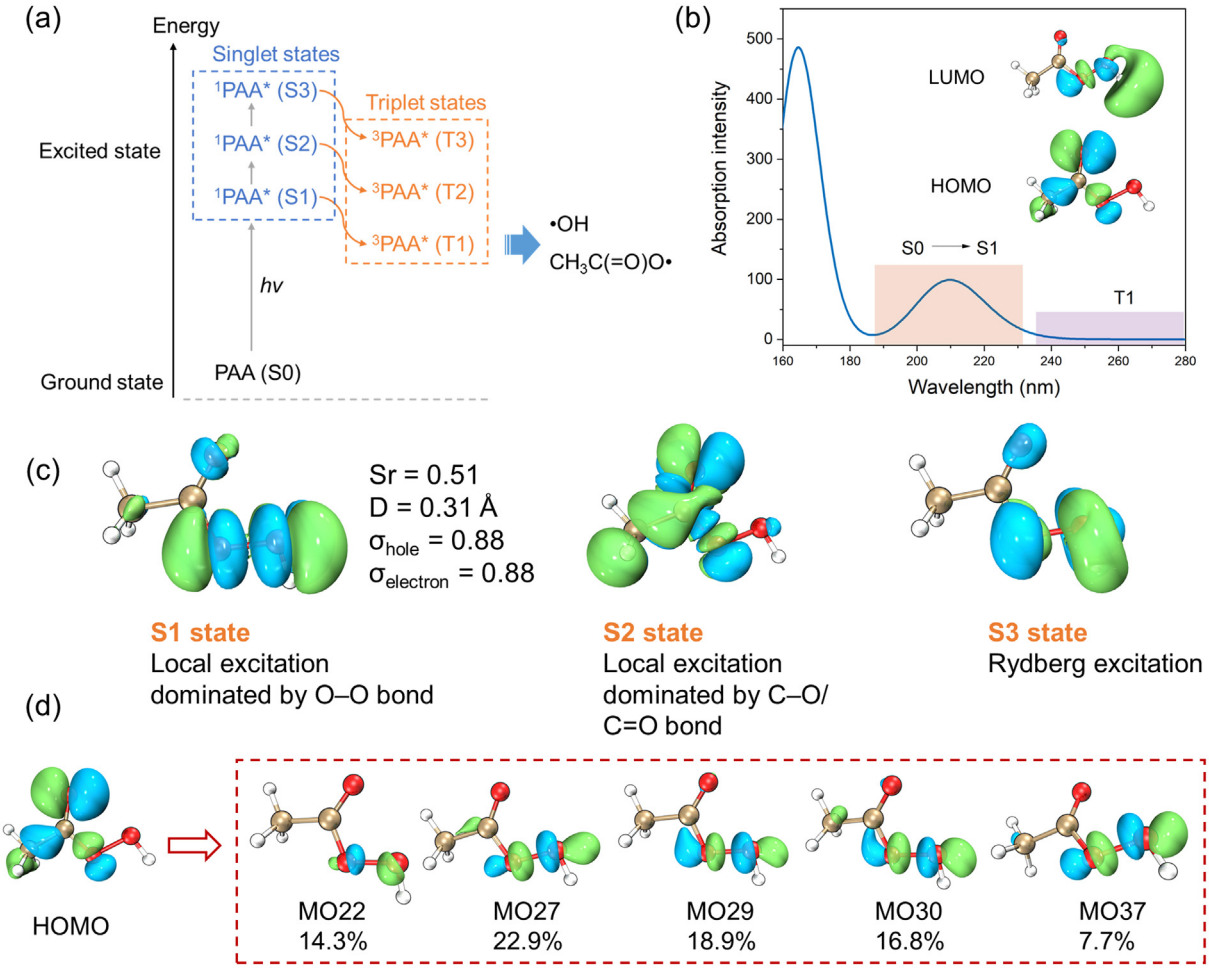

Fig. 2. DFT calculation for the excited states of PAA. (a) Schematic diagram of excited states (singlet states and triplet states) in UV-induced PAA activation system. (b) Simulated UV–vis spectra of PAA molecule calculated by TDDFT at the B3LYP/aug-cc-PVTZ level. (c) Calculated the isosurface of transition density, S_r index, as well as integral of hole and electron of the first excited singlet state (S1), second excited singlet state (S2) and third excited singlet state (S3) of PAA (isosurface = 0.001, the positive and negative phase parts of the orbital wave function are represented in blue and green, respectively). Sr index is determined to measure the degree of overlap between holes and electrons of S1 state; σ index is determined to measure the overall distribution breadth of holes or electrons of S1 state; D index is determined to measure the distance between the center of mass of holes and electrons of S1 state. (d) The contribution of major molecular orbital (MO) transition in the S1 state (isosurface = 0.05), where MO22, MO27, MO29, MO30 and MO37 are the molecular orbitals higher than HOMO.

(14.3%) and MO37 (7.7%) are considered as the predominant contribution for the similar overlapping orbitals.

$$CH_3C(=O)OOH \xrightarrow{UV} CH_3C(=O)OOH^* \text{ (excited state)} \quad (8)$$

Based on the light-induced PAA activation mechanism above, it is known that the wavelength of UV light obviously affects PAA activation due to the difference in photon energy. Then, radical production behaviors were compared using UV lights with different primary wavelengths (185, 254, and 365 nm). Compared with UV_{254}/PAA system, the signal of DMPO-·OH in UV_{185}/PAA system was greatly enhanced (Fig. 1h). Generally, the high molar extinction coefficient of UV_{185} for H_2O (1.53 cm^{-1}) leads to violent reactions in water, including homogeneous cleavage and photoionization of H_2O molecule, leading to efficient production of ·OH, hydrogen atoms (·H) and hydrated electrons (e_{aq}) (Eqs. (9)–(10)) [14]. Besides PAA activation, ·OH in UV_{185}/PAA system could also be produced through H_2O_2 activation and water photolysis [14]. DMPO-·CH_3 was also detected in UV_{185}/PAA system, with a lower signal intensity than that in UV_{254}/PAA system (Fig. 1h). This may be attributed to fewer photons being used for the cleavage of the peroxy bond (Eqs. (1) and (4)), where high-energy photons can also break other bonds in PAA or the coexisting H_2O_2/H_2O molecules [5]. In addition, the signal of DMPO-·OH was relatively lower in UV_{185}/H_2O_2 system than in UV_{185}/PAA system (Fig. S6a online), further demonstrating the efficient activation of PAA than H_2O_2. In TBA solution, a weak signal assigned to DMPO-$CH_3C(=O)OO$· was also captured in UV_{185}/PAA system (Fig. 1i). Moreover, two groups assigned to DMPO oxides were observed, i.e., DMPOO and DMPO-OR (Fig. S7b online). DMPOO (A_N = 15.5 G, g = 2.0059) was the photoinduced oxidation product (Fig. 1i), assigned to the reactivation reaction of DMPO-$CH_3C(=O)OO$·, because the similar peroxy bond also can be activated by UV light (Fig. S7a online). DMPOO-OR ("OR" represents open ring) was the product of DMPOO after the ring-opening reaction, and was ascribed to the oxidation of DMPOO or the oxidation of DMPO-$CH_3C(=O)OO$· (Fig. S7a online), with a very small hyperfine coupling constant (A_N = 8.0 G, g = 2.0070) for the offset of g-value (Fig. S6b online). The emergence of DMPO oxides only indicated an oxidative environment was formed after PAA activation, but cannot imply the formation of any radicals [11,15]. Similarly, the DMPOO signal was observed in the ethanol solution. The captured DMPO-CH_3·CHOH signal (A_N = 15.2 G, A_H = 21.8 G, standard spectrum simulated in Fig. S6c online) was assigned to the hydrogen atom

abstraction products of PAA via radical attack by ·OH, $CH_3C(=O)OO·$ and $CH_3C(=O)O·$ under photoinduction. Moreover, DMPO-$CH_3·C(=O)$ (A_N = 14.5 G, A_H = 17.8 G) was also captured in the ethanol solution, which was an unsaturated carbonyl carbon-centered radical. Thus, it is indicated that UV_{185} with higher photon energy (6.70 eV) can break C–O bond in PAA, resulting in the generation of $CH_3·C(=O)$ (Eq. (11)). In comparison, UV_{254} with lower photon energy (4.88 eV) cannot mediate this reaction. The existence of carbonyl group in $CH_3·C(=O)$ reduced the hyperconjugation effect, leading to a small A_H lower than 21.0 G. For the PAA activation mechanism, the electron transition induced by UV_{254} is attributed to the local excitation from non-bonding orbital to π^* orbital dominated by S1 state (Fig. 2c). In contrast, the transition induced by UV_{185} is ascribed to the C–O/C=O group transition and Rydberg excitation dominated by S2 state (7.17 eV, 172.9 nm) and S3 state (7.37 eV, 168.2 nm), respectively (Fig. S8 online). This is because of the higher photon energy and more efficient light absorption (Fig. S4 online). The BDE of the C–O bond is calculated as 79.5 kcal mol^{-1} (3.45 eV) (Fig. S3 online), which is much lower than the photo-energy of UV_{185} light. Then, the formation of S2 state results in the cleavage of C–O bond to generate $CH_3·C(=O)$, where the hole-electron separation is feasible. Meanwhile, the Rydberg excitation to S3 state can also lead to the generation of ·OH and $CH_3C(=O)O·$, where the hole and electron are distributed in the peroxy bond (Fig. 2c). In comparison, in UV_{365}/PAA system, only DMPO-·OH signal with lower intensity was observed (Fig. 1h and Fig. S6d online), because low activation efficiency for PAA occurred due to the much lower photon energy of UV_{365} (3.40 eV).

$$H_2O \xrightarrow{UV_{185}} ·OH + H· \quad (9)$$

$$H_2O \xrightarrow{UV_{185}} ·OH + H^+ + e_{aq}^- \quad (10)$$

$$CH_3C(=O)OOH \xrightarrow{UV_{185}} CH_3·C(=O) + ·OOH \quad (11)$$

In conclusion, we established an *in-situ* EPR detection method for accurate identification of the radicals generated in typical UV/PAA activation systems, combined with DFT calculation to deeply explain the generation mechanism of radicals. The concentration and type of radicals are dominated by photo-energy levels, namely light wavelength. The formation of ·OH, $·CH_3$ and $CH_3C(=O)OO·$ in UV_{254}/PAA and UV_{185}/PAA systems was directly confirmed by EPR spectra obtained in water or organic solvents. In addition, ·OH and the specific $CH_3·C(=O)$ with higher concentrations were tracked in UV_{185}/PAA system. In comparison, only ·OH with a much lower concentration was detected in UV_{365}/PAA system. Different radical behaviors in the UV/PAA systems are attributed to the difference in local excitation (254 nm) and Rydberg excitation (185 nm) mechanism. The identification of $CH_3·C(=O)$ and ·OH with higher concentrations in the UV_{185}/PAA activation system is valuable for advancing the practical application of vacuum UV-induced AOPs in water treatment area. The integration of DFT calculations with EPR detections provides deep insights into the identification and generation mechanism of radicals in PAA-based AOPs, instructing the regulation of radicals for specific organic pollutants degradation.

Conflict of interest

The authors declare that they have no conflict of interest.

Acknowledgments

This work was supported by the National Natural Science Foundation of China (52270053 and 52200083), the National Key Research and Development Program of China (2021YFA1202500), the Beijing Natural Science Foundation (8232035), the Beijing Nova Program (20220484215), the Beijing National Laboratory for Molecular Sciences (BNLMS2023011), the Emerging Engineering Interdisciplinary-Young Scholars Project (Peking University), and the Fundamental Research Funds for the Central Universities. DFT calculations supported by the High-Performance Computing Platform of Peking University and the National Key Scientific and Technological Infrastructure project "Earth System Numerical Simulation Facility" (EarthLab) are also acknowledged.

Author contributions

Long Chen and Wen Liu designed the research. Long Chen, Ruohan Zhang, Boyu Huang, and Zhaoli Liu performed the research and wrote the manuscript. Long Chen and Fan Li contributed to DFT data analysis. Wen Liu contributed to language polishing and visualization. All authors contributed to the discussion of the manuscript.

Appendix A. Supplementary material

Supplementary data to this article can be found online at https://doi.org/10.1016/j.scib.2025.03.008.

References

[1] Hodges BC, Cates EL, Kim J. Challenges and prospects of advanced oxidation water treatment processes using catalytic nanomaterials. Nat Nanotechnol 2018;13:642–50.
[2] Ao X, Eloranta J, Huang C, et al. Peracetic acid-based advanced oxidation processes for decontamination and disinfection of water: a review. Water Res 2021;188:116479.
[3] Chen F, Sun Y, Huang X, et al. Embedding electronic perpetual motion into single-atom catalysts for persistent Fenton-like reactions. Proc Natl Acad Sci USA 2024;121:e2314396121.
[4] Zhang T, Huang C. Modeling the kinetics of UV/peracetic acid advanced oxidation process. Environ Sci Technol 2020;54:7579–90.
[5] Yin R, Ruan X, Peng J, et al. Control of micropollutants in water by far-UVC photolysis of peracetic acid. Environ Sci Technol Lett 2024;11:759–63.
[6] Cai M, Sun P, Zhang L, et al. UV/peracetic acid for degradation of pharmaceuticals and reactive species evaluation. Environ Sci Technol 2017;51:14217–24.
[7] Yang S, Sun S, Xie Z, et al. Comprehensive insight into the common organic radicals in advanced oxidation processes for water decontamination. Environ Sci Technol 2024;58:19571–83.
[8] Wu J, Yu H. Confronting the mysteries of oxidative reactive species in advanced oxidation processes: an elephant in the room. Environ Sci Technol 2024;58:18496–507.
[9] Liu T, Xiao S, Li N, et al. Water decontamination via nonradical process by nanoconfined Fenton-like catalysts. Nat Commun 2023;14:2881.
[10] Wu J, Yang T, Sun Y, et al. Tailoring the selective generation of oxidative organic radicals for toxic-by-product-free water decontamination. Proc Natl Acad Sci USA 2024;121:e2403544121.
[11] Chen L, Duan J, Du P, et al. Accurate identification of radicals by *in-situ* electron paramagnetic resonance in ultraviolet-based homogenous advanced oxidation processes. Water Res 2022;221:118747.
[12] Ghosh S, Verma P, Cramer CJ, et al. Combining wave function methods with density functional theory for excited states. Chem Rev 2018;118:7249–92.
[13] Liu Z, Lu T, Chen Q. An sp-hybridized all-carboatomic ring, cyclo [18] carbon: electronic structure, electronic spectrum, and optical nonlinearity. Carbon 2020;165:461–7.
[14] Chen B, Huang Y, Zhang Q, et al. Formation of nitrite and hydrogen peroxide in water during the vacuum ultraviolet irradiation process: impacts of pH, dissolved oxygen, and nitrate concentration. Environ Sci Technol 2021;55:1682–9.
[15] Wu J, Yang T, Chen F, et al. Unexpected side reactions dominate the oxidative transformation of aromatic amines in the Co(II)/peracetic acid system. PNAS Nexus 2024;3:pgae040.